https://doi.org/10.5194/egusphere-2026-204
Preprint. Discussion started: 28 January 2026

Novel method to locate and quantify point-source methane emissions using time series of ground-based column observations

Friedrich Klappenbach[1], Jia Chen[1], Moritz Makowski[1], Andreas Luther[1], Ronald C. Cohen[2], Jonathan E. Franklin[3], Steven Wofsy[3], and Taylor Jones[3,4]

[1]Environmental Sensing and Modeling, Technical University of Munich (TUM), Munich, Germany
[2]Chemistry Earth & Planetary Science, UC Berkeley, Berkeley, United States
[3]Harvard John A. Paulson School of Engineering and Applied Sciences, Harvard University, Cambridge, MA, USA
[4]George Town University 360, Georgetown , United States

Correspondence: Friedrich Klappenbach (friedrich.klappenbach@gmail.com)

Abstract. Identifying and quantifying local methane emitters remains a major challenge for atmospheric monitoring. We present a novel top-down method to estimate both the upwind location and emission strength of an unknown atmospheric source from a time series of concentration observations. The approach employs backward trajectories from a Lagrangian Particle Dispersion Model (LPDM) to derive a characteristic transfer function for each potential source region. The transfer function that best reproduces the observed enhancement identifies the most likely source location. In a second step, the emission strength is inferred from the particle ensemble and its corresponding surface footprint.

The method was developed and tested using data from a six-week measurement campaign in the San Francisco Bay Area, where six EM27/SUN near-infrared Fourier transform spectrometers were operated as part of a collaborative effort to quantify greenhouse gas emissions. At the UC Berkeley site, one instrument recorded a strictly periodic methane enhancement of approximately 10 ppb occurring every 12 minutes. Since co-emitted species showed no correlation with this pattern, the signal was attributed to a single, point-like, puff-emitting methane source.

Favourable meteorological conditions enabled the analysis of several enhancement peaks. The retrieved average emission strength during the emission episodes was 0.8 - 78 g CH_4 s^{-1} (equivalent to 2.1 - 190 metric tons yr^{-1}). Although the exact source could not be identified in the field, the emission characteristics are consistent with periodic natural-gas venting from a heating system with an installed power output of approximately 500-1000kW installed power. The study demonstrates the potential of this approach for detecting and characterising local methane emitters from ground-based remote-sensing observations.

1 Introduction

Methane (CH_4) is a potent greenhouse gas with a global warming potential (GWP) about 28 times that of carbon dioxide (CO_2) on a 100-year timescale (Myhre et al., 2013), and roughly 84 times higher when evaluated over 20 years. Given its high short- and long-term warming potential, accurate quantification of methane emissions is critical for both near-term climate mitigation and long-term carbon budgeting. While anthropogenic CO_2 accounts for more than 75 % of global greenhouse gas emissions and can be estimated with an uncertainty of about 20 %, global CH_4 emissions (contributing roughly 19 %) remain considerably more uncertain, with typical uncertainties near 30 % (Solazzo et al., 2021).

Atmospheric emissions are generally estimated using two complementary approaches. *Bottom-up* methods quantify individual sources and scale their activity to regional or national inventories (e.g. Hegarty et al., 2007; Subramanian et al., 2015; Thorpe et al., 2020; Lebel et al., 2022). *Top-down* methods, in contrast, infer source strengths and locations from atmospheric observations through inverse modelling (e.g. Fairley and Fischer, 2015; Desjardins et al., 2018; Schneising et al., 2014; Chen et al., 2016). Methane emissions are often unintentional—originating from fugitive leaks, landfills, or livestock (e.g. Hopkins et al., 2016; Enishi, 2007)—and therefore difficult to constrain by bottom-up inventories alone, motivating the use of combined or hybrid approaches (e.g. Mønster et al., 2019; Lassey, 2008; Jones et al., 2021).

From an observational perspective, top-down methods rely either on *in situ* measurements or on remote sensing. *In situ* data can be collected continuously at fixed stations or from mobile platforms (e.g. Xueref-Remy et al., 2020; Al-Shalan et al., 2022; Chen et al., 2020), or as discrete samples such as flasks or air cores for later laboratory analysis (e.g. Andersen et al., 2021; Young et al., 2023; Dietrich et al., 2023). Remote sensing techniques, on the other hand, provide spatially integrated observations either from satellites (e.g. Hu et al., 2016, 2018; Hamburg et al., 2022) or from ground-based Fourier-transform spectrometers (e.g. Wunch et al., 2015; Frey et al., 2019; Dietrich et al., 2021). These ground-based systems measure the total atmospheric column along the instrument line of sight and thus deliver temporally resolved, but spatially integrated, concentration data.

A major challenge in top-down emission estimates for long-lived gases is the definition of the background concentration. Observed signals contain both local enhancements and a substantial pre-existing atmospheric background. High-frequency time-series often estimate the background as a low-percentile of the observations (e.g. the lowest 10 %; Ammoura et al., 2016; Barkley et al., 2017; Cui et al., 2017), or use dedicated background sites with minimal local influence (e.g. Viatte et al., 2017; Karion et al., 2019). Spatially resolved satellite observations instead identify background regions within the swath (e.g. Makarova et al., 2020; Shekhar et al., 2020; Hamburg et al., 2022). Alternatively, model-based backgrounds can be derived from atmospheric transport simulations (e.g. Vogel et al., 2019).

Most of the above approaches employ transport models of varying complexity to determine source–receptor relationships or footprint sensitivities. In standard inverse frameworks, these footprints are combined with spatially resolved emission inventories to drive a forward model (e.g. Jones et al., 2021; Luther et al., 2019; Forstmaier et al., 2023; Wu et al., 2018).

However, such footprints are typically computed independently for each observation time step, without explicitly representing their joint temporal structure. Several studies, including (e.g. Patel et al., 2025), have exploited the temporal evolution of observed methane plumes—whether through imaging spectroscopy, empirical plume-spread models, or time-resolved inversions—to constrain source characteristics. These approaches use the temporal development of the plume field itself, rather than the temporal structure inherent in the back-trajectories. In contrast, our framework interprets the upstream trajectories as the impulse response of a linear time-invariant system, enabling us to exploit their full temporal dimension in a principled, system-theoretic manner to infer source distances.

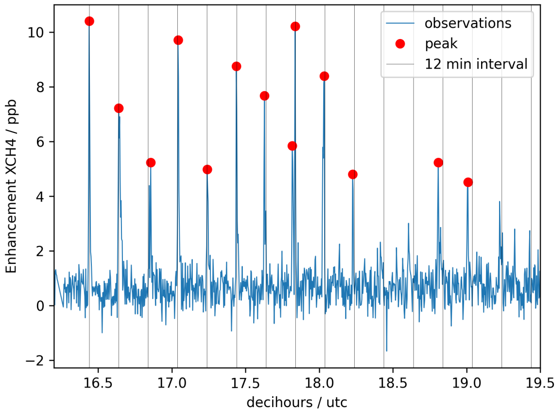

Figure 1. Enhancements of methane total column during the forenoon on Nov. 3$^{\text{rd}}$ 2016 at UC Berkeley. The enhancement is calculated by subtracting the 10% quantile in a 60 minute rolling window. For reference a 12 minute pattern is plotted (vertical lines) which aligns well with the observed enhancements.

In this study we present a top-down approach that analyses a time-series of ground-based remote-sensing observations. The method uses the travel time of simulated particles to estimate the enhancement pattern that a point-like source would produce in the measured concentration record. We describe this process within the framework of linear, time-invariant (LTI) system theory, where the atmospheric transport can be represented by a transfer function, or impulse response, $h(t)$, that characterises the system behaviour without detailed knowledge of its internal structure. This black-box treatment enables the derivation of source distance and emission strength directly from observed peaks, offering a compact yet physically interpretable alternative to traditional inversion techniques.

2 Methodology

This section describes the framework developed to estimate the location and strength of a local methane source from ground-based remote-sensing observations. The method combines linear system theory with a Lagrangian particle dispersion model (LPDM), treating the atmospheric transport as a linear time-invariant (LTI) system. In the following, we outline the conceptual background, observational dataset, model configuration, and inversion procedure. For a brief introduction into LTI systems within this context please refer to Appendix A.

2.1 Observational data

The method was tested using total column observations obtained during a six-week campaign in autumn 2016 in the San Francisco Bay Area, USA. At the UC Berkeley site (37.876° N, 122.257° W, 119 m a.s.l.), a Bruker EM27/SUN near-infrared Fourier transform spectrometer was operated continuously during sunshine conditions (Gisi et al., 2011, 2012; Hase et al., 2016; Chen et al., 2016; Frey et al., 2019). Interferograms were recorded approximately every 12 s and processed with the `proffast 2.2` software (Frey et al., 2019; Sha et al., 2020; Feld et al., 2024; Makowski et al., 2025; Hase, 2025) to retrieve total column-averaged dry-air mole fractions of methane ($X_{\mathrm{CH_4}}$), carbon dioxide ($X_{\mathrm{CO_2}}$), water vapour ($X_{\mathrm{H_2O}}$), and oxygen ($X_{\mathrm{O_2}}$).

During the morning of 3 November 2016, the instrument detected periodic methane enhancements with a 12-minute recurrence and amplitudes of approximately 10 ppb above background. Background concentrations were defined as the rolling 10 % quantile of a 60-minute window centered on each measurement (see Figure 1). The choice of the window-size is found to be uncritical, due to the prominence of the peaks. Please refer to Appendix B for details on co-emitted species and an assessment of observational uncertainties.

2.2 Conceptual framework

In atmospheric inverse modelling, the goal is to infer the emission signal $e(t)$ from an observed concentration enhancement $y(t)$. Following the theory of linear time-invariant systems, the atmosphere can be represented as a system that transforms an input $e(t)$ (emission) into an output $y(t)$ (measured enhancement) through convolution with an impulse response or *transport kernel* $k(t)$:

$$y(t) = (e * k)(t) = \int_{-\infty}^{\infty} e(\tau)\,k(t-\tau)\,d\tau. \tag{1}$$

Here, $k(t)$ encapsulates the temporal and spatial characteristics of atmospheric transport between the source region and the observation site. In this framework, identifying a source corresponds to finding the kernel that best reproduces the observed signal and determining the corresponding emission strength. We employ a two step approach:

1. derive maximum source distance r_{max}

2. infer the emissions from potential candidates within that range.

2.3 Atmospheric transport modelling

Atmospheric transport was simulated using the Hybrid Single-Particle Lagrangian Integrated Trajectory (HYSPLIT) model (Stein et al., 2015) running the Stochastic Time-Inverted Lagrangian Transport (STILT) model (Lin et al., 2003; Fasoli et al., 2018; Loughner et al., 2021) transport formulation.

Local observations indicate stable transport conditions over several hours. Backward trajectories were launched every 15 minutes from 10 receptor points distributed along the instrument's line of sight up to 100 m above ground level. For each receptor, 500 particles were tracked backward in time, in one minute steps. The used meteorological fields are from NOAA's High-Resolution Rapid Refresh (HRRRv1) reanalysis model at 3 km × 3 km spatial resolution for every hour (Benjamin et al., 2016a, b). The ensemble of particle positions forms the basis for constructing the *transport kernel*.

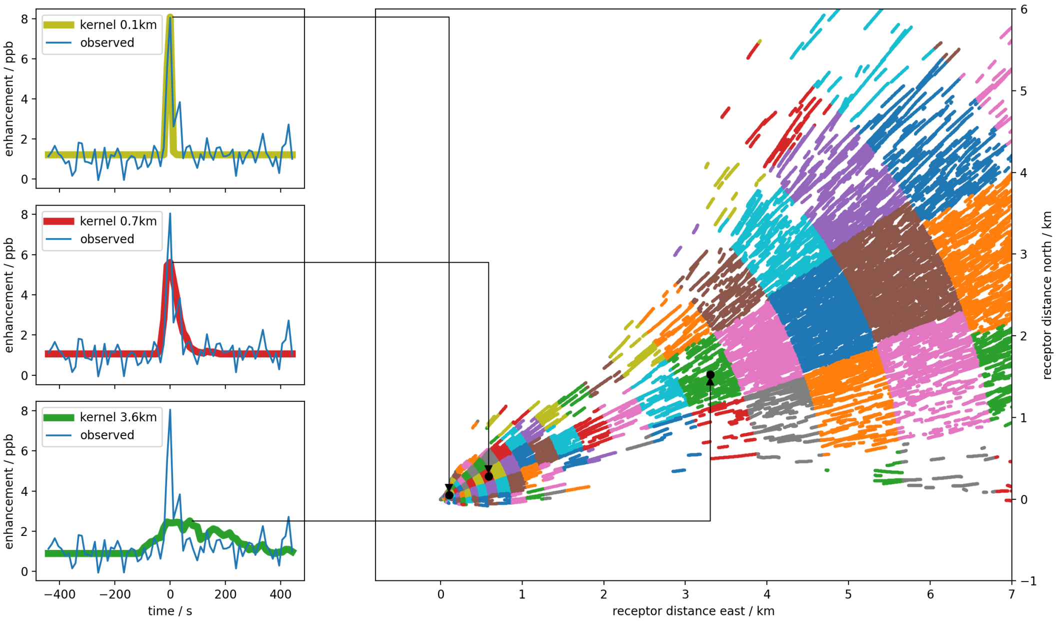

Figure 2. Illustration of the particle segmentation and range estimation procedure. **Right:** Top view of consecutive STILT-simulated particle positions in the spatial domain. Particles are released from the receptor at $(0,0)$ and traced backward in time; in this case the wind originates from the east–northeast. Each particle is assigned to an ensemble $P_{i,j,k}$ defined by upwind distance i, wind-relative azimuth j, and source altitude above ground k, indicated by different colors. Only one source altitude (k) is shown here. **Left:** Scaled histograms of particle arrival times for selected segments (thick colored lines), representing the respective transport kernels. The maximum upwind source distance ($\approx$ 0.7 km in this example) corresponds to the kernel which best fits the observed enhancement (see. Section 2.5).

2.3.1 Discretisation of the upwind domain

To construct the transport kernel, the upwind domain sampled by all backward trajectories is divided into discrete volumetric segments according to upwind distance, wind-relative azimuth, and altitude. Each segment is indexed by (i,j,k), representing its radial (i), angular (j), and vertical (k) position, respectively. All particles passing through a segment form the corresponding *particle ensemble* $P_{i,j,k}$. For each ensemble, the residence times are accumulated to derive the surface sensitivity, which serves as the building block for the transport kernel (see Section 2.4).

A schematic of this segmentation is shown in Figure 2, illustrating how the domain is partitioned into radial and angular bins relative to the prevailing wind direction. A detailed mathematical description of the binning procedure and coordinate transformations is provided in Appendix E.

2.4 Transport kernel construction

To relate emissions within the upwind domain to the observed signal, we derive a time-resolved *transport kernel* $k(t)$ from the ensemble of STILT trajectories. Each trajectory records the residence time of particles within discrete spatial cells of the model domain. Following Lin et al. (2003), the surface sensitivity (footprint) for a particle ensemble in cell i,j,k is

$$f_{i,j,k}(t) = \frac{\Delta t_{\mathrm{sim}}\, m_{\mathrm{air}}}{\Delta z_k\, \rho_{i,j,k}}, \tag{2}$$

where Δt_{sim} is the model time step, m_{air} the molar mass of air, $\rho_{i,j,k}$ the mean air density in the cell, and Δz_k the segments vertical thickness, we use 10 m. The kernel is then formed as a weighted histogram t_m with bin-size of Δt_h of particle arrival times:

$$k_{i,j,k}(t_m) = \sum_{p \in P_{i,j,k,q}} \chi(t_m)\, f_{i,j,k,p}(t)\, w(n_q, A_q), \tag{3}$$

$$\chi(t_m) = \begin{cases} 1, & \text{if } t \in [t - \frac{\Delta t_h}{2}, t + \frac{\Delta t_h}{2}) \\ 0, & \text{else} \end{cases} \tag{4}$$

where $w(n_q(z_r), A_q(z_r,t_r))$ is a dimensionless receptor-specific weighting function. This function assigns a weight to each of the receptor points q along the instruments line of sight. It accounts for the number of particles $n_q(z_r)$ the receptor point represents at the receptor altitude z_r, as well as the instruments specific averaging kernel $A(z_r,t_r)$ at the receptor time t_r (see Appendix D). Thus, $k_{i,j,k}(t)$ represents the system's impulse response for a given particle ensemble $P_{i,j,k}$: the temporal pattern expected at the receptor for a unit emission released within the corresponding 3-D upwind segment. The unit of k is $ppm \cdot m^2 s/\mu mol$ - the footprint unit.

2.5 Step 1: Source-range estimation

For each upwind segment $s := (i,j,k)$, we compare the modeled kernel $k_s(t)$ to the observed enhancement $y(t)$. A least-squares fit is applied with three free parameters—a temporal shift τ_s, an amplitude a_s, and an offset o_s:

$$\min_{\tau_s, a_s, o_s} \| y(t) - a_s\, k_s(t+\tau_s) - o_s \| . \tag{5}$$

The goodness of fit is quantified by the standard deviation of the residuals,

$$\rho_s = \mathrm{std}[y(t) - a_s\, k_s(t+\tau_s) - o_s], \tag{6}$$

with lower values indicating a better temporal match. The distance at which ρ_s is minimal defines the furthest upwind location of the source ($r_{\max}$) ; segments beyond this distance produce kernels too broad to reproduce the observed narrow peaks.

https://doi.org/10.5194/egusphere-2026-204
Preprint. Discussion started: 28 January 2026

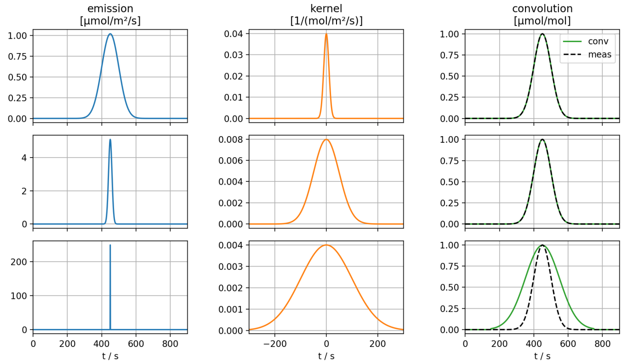

Figure 3. Illustration of the connection between source emission patterns and the transport kernel and the ovserved enhancement. From left to right: A source emission pattern (blue) is transported and diluted according to the kernel (orange), resulting in a predicted downwind enhancement (green), which can be compared to an observed signal (black, dashed). From top to bottom: Scenarios with increasing upwind distance. The same enhancement can be explained with a long emission duration (top) but requires a narrow transport kernel. With increasing upwind distance, the kernel broadens and requires a shorter emission duration to explain the same enhancement. In the bottom row, even a puff-like emission cannot explain the observed enhancement, indicating that the source lies beyond the maximum upwind influence range.

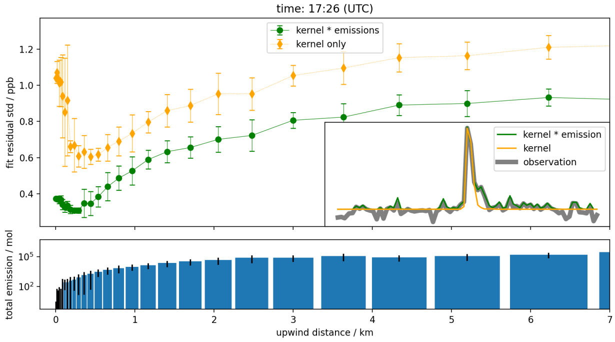

Figure 4. Illustration of the range estimation method for the methane enhancement observed at 17:26 UTC. **Top:** Standard deviation of the fit residuals, ρ_i (ppb), as a function of upwind distance (km). A distinct minimum at approximately 0.7 km indicates the most likely maximum distance to the emission source. **Center right:** Observed methane enhancements (gray) and two fitted reconstructions using kernels corresponding to distances near the residual minimum. The kernel–emission convolution (green) reproduces the observed enhancement, highlighting the physical constraint on the solution. **Bottom:** Corresponding median emission strength (mol), assuming the source is located within the respective upwind segment. Because the inferred emission increases strongly with distance, the vertical axis is shown on a logarithmic scale.

https://doi.org/10.5194/egusphere-2026-204
Preprint. Discussion started: 28 January 2026

2.6 Step 2: Emission strength inversion

Now, that $r_{\max}$ is obtained the most likely source region can be identified in the upwind sections closer or equal $r_{\max}$. For this location the time-resolved emission rate $e(t)$ can be retrieved by solving a non-negative least-squares problem:

$$\min_{e(t)\geq 0} \| y(t) - (k * e)(t) \| \tag{7}$$

This inversion yields the emission pattern that, when convolved with the transport kernel, best reproduces the observed enhancement. Figure 3 illustrates the principle how the emission-patterns evolve under multiple kernel-scenarios, given the same observed enhancement. The residual of both optimization problems (Eq. 5 and 7) are displayed in Figure 4. The residual obtained from Eq. 7 is generally lower than that of Eq. 5, as the emission strength is adjusted for a fixed kernel. However, the maximum upwind distance $r_{\max}$ is robustly identified only through Eq. 5, where the residual minimum reflects the physically consistent kernel extent.

Finally, the integration of $e(t)$ over the emission period provides the total emitted mass for each segment:

$$E = \int e(t)\, dt. \tag{8}$$

Negative values are not permitted, ensuring physical plausibility and preventing artefacts that could compensate for excessively wide kernels. The resulting emission map therefore contains only non-zero fluxes in dynamically consistent upwind regions.

2.7 Uncertainty analysis

Uncertainties in the retrieved emissions arise from both the inversion procedure itself and from systematic errors in the input data. For the method-intrinsic part, we use the ensemble of all upwind segments defined by distance, azimuth, and altitude. Only well-sampled segments—those contributing significantly to the total surface sensitivity—are retained. The ensemble mean and the range spanned by the retained members provide a first-order estimate of the methodological uncertainty.

Systematic errors are dominated by uncertainties in the meteorological wind field, which directly affect the surface sensitivity and therefore the inferred emission strength. An error in the mean wind speed σ_u/u propagates approximately linearly to the emission estimate,

$$\Delta E \approx E \cdot \frac{\sigma_u}{u}. \tag{9}$$

Based on comparisons with local meteorological observations, wind speed errors during the analysed period are estimated at below 50 %, which translates a similar uncertainty in the derived emissions. We correct modeled emissions by the deviation in wind speed according to equation 9. Further details on the can be found in Appendix G.

Observation noise adds an additional, smaller contribution. Because the emission rate is obtained by integrating concentration enhancements over time, random measurement noise is partly compensated, but longer integration windows can accumu-

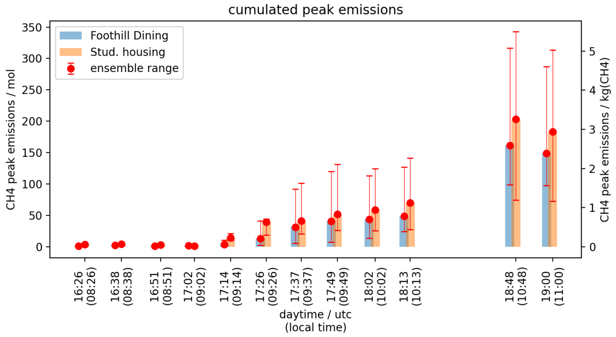

Figure 5. Retrieved emission estimates for the two potential source candidates (Student housings and the Foothill Dining). The results are corrected by wind-speed using the observed wind speed rather than the meteorological model solely. Te ensemble range is indicated by the error bars.

late additional uncertainty. This contribution tends to be positive, since negative emissions are excluded. We therefore treat observational noise as a secondary effect compared to wind-related errors.

Overall, we estimate a residual relative uncertainty of roughly 30–70 % for the retrieved emission strengths, dominated by the uncertainty in the wind speed changes due to surface roughness and by ensemble variability. This uncertainty can significantly increase if the deviation of the meteorological model to the present conditions cannot be derived.

3 Results

The potential source areas were identified using the optimised particle ensemble $P_{\mathrm{opt}}(\mathrm{lat},\mathrm{lon})$, constructed from the best-fitting trajectories for each of the 13 forenoon enhancement peaks. Figure 6 overlays these ensembles on a high-resolution map of the surrounding area. Possible emitters are located within the region marked by bluish points, which correspond to low model–observation residuals in the range-estimation fit (see Section 2.5). Red areas indicate poorer agreement and thus less likely source locations.

The emission characteristics suggest a direct, periodic release of natural gas into the atmosphere rather than a diffuse ground-level leak. Several upwind facilities were investigated as potential emitters. A natural gas valve located farther east was not equipped with a blow-down vent. The nearby Lawrence Berkeley National Laboratory (LBNL) uses steam supplied from a cogeneration plant rather than direct gas combustion, and the two smoke stacks located roughly 800 m upwind would imply unrealistically large emissions. The most plausible candidates are therefore natural gas powered units of the Foothill Dining and Foothill Student Housing complexes. Google Street View imagery indicates the presence of a natural gas–fired boiler. A plausible explanation is a burner that fails to ignite and automatically purges its combustion chamber every 12 minutes, releasing unburned gas to the atmosphere. Assuming a typical installed heating capacity of 500–1000 kW for buildings of this size, the corresponding methane consumption would be on the order of 8–16 g s^{-1}, consistent with the retrieved emission rates. Attempts to contact the facility management for confirmation were unsuccessful.

https://doi.org/10.5194/egusphere-2026-204
Preprint. Discussion started: 28 January 2026

Table 1. Ensemble-averaged methane emission estimates for two potential upwind source locations. *Annual values assume five emission events per hour throughout the entire year.

Source candidate	Mean (min/max)	Unit
Foothill Dining	28.2 (0.8 / 77.9)	g s^{-1}
Student Housing	38.1 (0.9 / 78.4)	g s^{-1}
Foothill Dining	1.20 (0.05 / 3.72)	kg per peak
Student Housing	1.53 (0.05 / 4.33)	kg per peak
Foothill Dining	52.7 (2.1 / 162.9)	t CH_4 yr^{-1} *
Student Housing	66.8 (2.0 / 189.5)	t CH_4 yr^{-1} *

Figure 5 shows the retrieved emission strength corresponding to each observed enhancement peak during the forenoon. For the most likely source candidate located about 146 m upwind, the individual peaks yield consistent emission magnitudes after wind-speed correction. On average, we obtain values between 0.8 g s^{-1} and 78 g s^{-1} per event, corresponding to roughly 0.05–4 kg per release.

Table 1 summarises the ensemble-averaged results for the two most plausible upwind source locations. Upscaling to annual values assumes a regular pattern of five emission events per hour (one every 12 minutes).

4 Conclusions

We have developed a novel top-down approach to identify potential source regions and emission strengths from peak-like enhancements in atmospheric trace gas observations. The method employs a Lagrangian particle ensemble to derive the characteristic transfer function of each potential source region. STILT-generated footprints indicate potential source regions several tens of kilometers upwind. By using high-resolution four-dimensional meteorological fields—primarily wind speed and direction—and comparing transport patterns with the observed enhancements, this method narrows the potential source region to within 1 km.

Although the present analysis focuses on total column methane observations, the approach is generally applicable to other pollutants and observational techniques that provide temporally resolved concentration data.

Our evaluation confirmed the consistency of both the observational and meteorological input data. The results show that the method is robust with respect to key configuration parameters, such as the choice of radial binning. Nevertheless, uncertainties remain substantial, mainly due to wind-field errors and observational noise. The accuracy of the meteorological model in terms of wind speed is particularly critical, as it directly determines the inferred emission strength. If observed meteorological data is not available as in this study, a high uncertainty needs to be assumed.

The approach is best suited for isolated, point-like, or short-term “puff” emitters. For sources that deviate from this assumption, the method tends to overestimate the source distance and consequently the emission strength, although it can still provide

https://doi.org/10.5194/egusphere-2026-204
Preprint. Discussion started: 28 January 2026

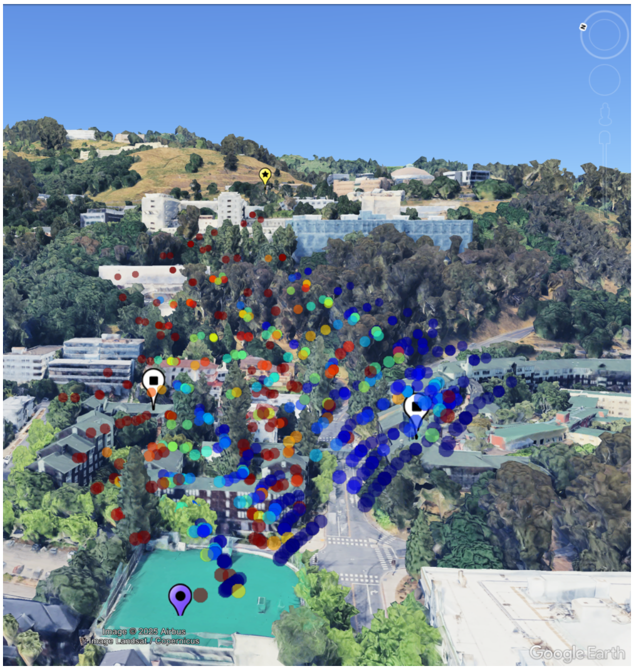

Figure 6. Top view facing east–northeast showing the optimised particle ensembles P^{*}_{opt} for all observed forenoon enhancements. The EM27/SUN observation site (purple marker) is located on the roof of the green building. The meteorological station LBNL1 (yellow marker) lies within the upwind direction. White markers denote potential source locations: Foothill Dining (right) and Student Housing (left). Dots represent the fit residuals of the forward model compared to observations—blue indicating low residuals (good agreement) and red high residuals. An increasing trend of residuals with upwind distance is apparent, supporting the localisation of the source within the bluish region. Google Earth. © Google, data provider: Image © 2025 Airbus / Image Landsat / Copernicus

a useful upper bound on the likely source range. Similarly, if a plume is only partially observed (e.g., the diluted outer section rather than the plume centre), the retrieved emission strength will be underestimated. Baseline noise in the observations can also broaden the apparent peak and bias the distance estimate.

Future work will focus on extending the method to more complex emission scenarios, including broader or overlapping peaks from stronger or more distant sources, and to quasi-continuous emitters with non-symmetric rise and decay times. Moreover, coupling with higher-resolution local meteorological models may further improve the localisation accuracy and the quantification of emission strengths.

Code availability. We plan to provide the code to public in a more generalized version.

Data availability. Can be provided upon request.

Appendix A: Linear Time Invariant Systems

We briefly introduce the concept of Linear Time-Invariant (LTI) systems from system theory, as it forms the conceptual foundation for our approach.

An LTI system is a model that maps an input signal $x(t)$ to an output signal $y(t)$ via a transformation H, such that

$$y(t) = H(x(t)).$$

Two key properties define LTI systems:

- **Linearity:** For any signals $x_1(t), x_2(t)$ and scalars α, β,

  $$H(\alpha x_1(t) + \beta x_2(t)) = \alpha H(x_1(t)) + \beta H(x_2(t)).$$

- **Time-invariance:** For any time shift τ, the system satisfies

  $$H(x(t-\tau)) = y(t-\tau).$$

Both aspects apply for our inverse problem. The linearity is trivial, because the the trajectory derived footprint f to a given enhancement y is is proportional to the emissions. The time-invariance is implicitly assumed with the use of backward-trajectories discussed in (Lin et al., 2003).

A fundamental result of system theory states that any LTI system can be fully characterized by its response to a Dirac delta function $\delta(t)$. The output $h(t) = H(\delta(t))$ is known as the *impulse response* of the system. Given this response, the output for an arbitrary input $x(t)$ is computed via convolution:

$$y(t) = (x * h)(t) = \int\limits_{-\infty}^{\infty} x(\tau) h(t-\tau)\, d\tau.$$

As a simplified real-world example, consider a thermometer that reacts sluggishly to rapid temperature changes. The true ambient temperature $x(t)$ is filtered by the device's physical response, producing a delayed observation $y(t)$. The impulse response $h(t)$ in this case reflects the thermal inertia of the thermometer.

LTI systems also play a central role in other domains. In optics, for instance, the impulse response is known as the *point spread function (PSF)* and describes how a point source of light is blurred by an optical system. The PSF can be used as a convolution kernel to model optical distortions such as defocus or aberrations.

In this study we adopt this LTI perspective for atmospheric transport modeling and interpret the ensemble of particle trajectories simulated by STILT as the impulse response of a LTI-system. Specifically, we assume a hypothetical instantaneous point source (i.e., a δ-emission) within a source region and track the particles' transport to the observation site. The footprint weighted arrival times then serve as a transfer function $h(t)$ that links emissions in space and time to observed concentrations. Given a observed peak-enhancement this approach allows not only to identify the maxium upwind source influence distance r_{max} but also the corresponding source emission pattern $e(t)$ and thus the overall emission.

https://doi.org/10.5194/egusphere-2026-204
Preprint. Discussion started: 28 January 2026

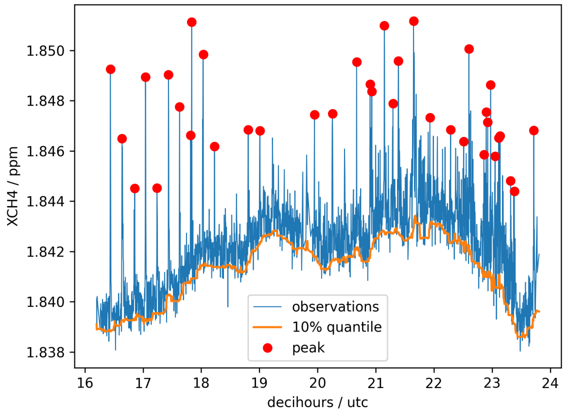

Figure B1. Observations of methane total column during the forenoon on Nov. 3rd 2016 at UC Berkeley. The enhancement is calculated by subtracting the 10% quantile in a 60 minute rolling window.

Appendix B: Observations

Figure B1 shows the observed total column average of methane of the entire day, together with the 10%-quantile as background: For each observation at the time step t_0, we define a 60-minute window with $dt = \pm 7.5$ minutes. The maximum value of the lowest 10 percent of these observations (Y) is assumed to be the background (Equation B1).

$$y_{bg,t_0} = \max\{y(t)|t_0 - dt > t \leq t_0 + dt \, \text{and} \, y(t) \in Y\} \tag{B1}$$

We consider the correction for the solar zenith angle as negligible, because of the broadband characteristic compared to the observed peak enhancements.

Figure B2 shows the enhancement calculated using the 10%-quantile as background $e = y - y_{bg}$.

As a measure for the precision of the spectroscopic total column average we use X_{air} as an indicator. X_{air} is the ratio of spectroscopic expected ground pressure and the observed hydro-static ground pressure. Note, that there are different definitions of X_{air}, we use the one (Frey et al., 2019) defines in section 3.3. Ideally X_{air} should scatter around one. Deviations from this value indicate shortcomings in the spectroscopic retrieval. Figure B3 shows the X_{air} parameter to be constant in the forenoon that day; thus, we consider only the peaks observed here as evaluable for our analysis.

Co-emitted species can give indicators to certain sources. Combustion-related processes might enhance CO_2 observations, whereas emissions from digesters might increase water vapor abundance. Figure B4 displays the retrieved species, which exhibit no correlation with the enhanced methane observations. One exception is the correlated rise of XCO_2 of 1ppm, approximately 20 seconds before the methane peak at $t = 17.6287$ hours which translates to 17:37:46 UTC. The reason for this enhancement in CO_2 remains unclear.

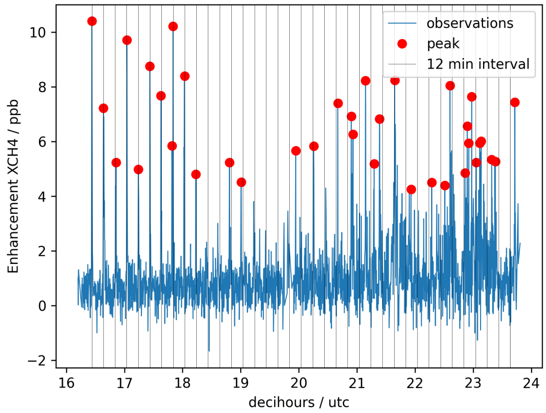

Figure B2. Observed total column enhancenets of methane on Nov 3rd.

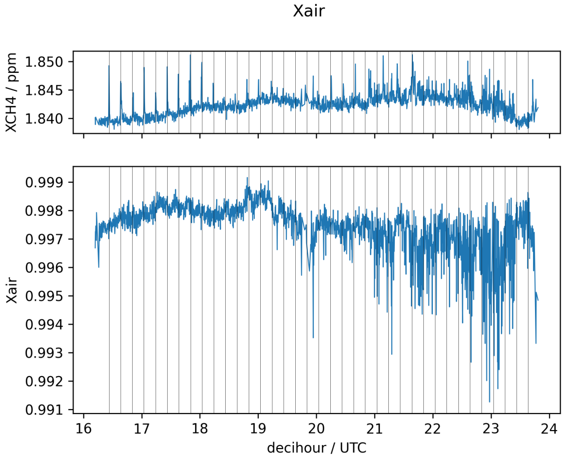

Figure B3. Observed methane total columns and X_{air} as an indicator of systematic errors. While X_{air} remains fairly constant in the forenoon, deviations begin to spike later in the day, reducing confidence in the observed methane total column observations.

To put the total column observations into perspective: 10ppb Enhancement in the total column is equivalent to approximately $3.5 \cdot 10^{-3}$ mol/m^2. If the plume has a height of only 10 m an in-situ instrument would measure additional 8400 ppb of Methane. A source with the strength of $7 \cdot 10^{-3}$ mol/s, located directly next to the total column instrument (1m lateral dilution) at wind-speeds of 2 m/s (roughly the observed wind speed that day) would create this enhancement. A plume with 30 m dilution width would be equivalent to 0.21 mol/s.

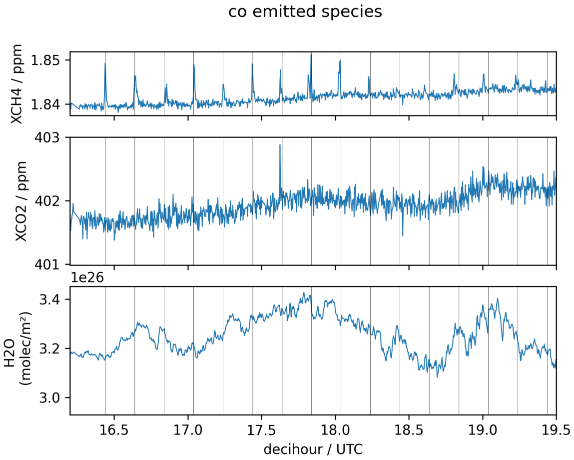

Figure B4. Observed total columns of possibly co-emitted species (CO_2 and H_2O). Both show no correlation whatsoever. This indicates a pure methane source.

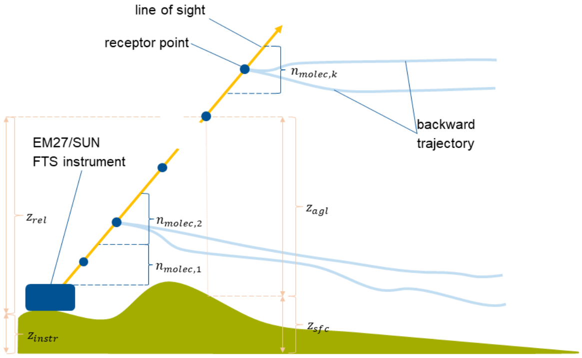

Figure C1. Schematic of the receptor points (blue dots) along the slant line of sight of the instrument. Four representative trajectories are shown in light blue, calculated backward in time. Vertical weighting w is based on the number of molecules $n_{molec,j}$ in the layer of representation, considering different surface elevations.

Appendix C: Receptor points and vertical weighting

270 We place four dimensional receptor points $p(x,y,z,t_{dw})$ along the line of sight as (Jones et al., 2021) suggested. x and y represent the longitude/latitude coordinate on the WGS84 grid in degrees, negative west of Greenwich, negative south of equator. t_{dw} represents the downwind time in julian date format. x and y are projected according to the solar position from the site location x_0, y_0, z_0 and z_{rel} altitude above the instrument. As altitude STILT accepts altitudes above ground level z_{agl}. In

https://doi.org/10.5194/egusphere-2026-204
Preprint. Discussion started: 28 January 2026

presence of complex topography the change in surface elevation on the projected $x-y$ coordinates cannot be neglected. We use the underlying STILT elevation and compute the the altitude at the projected point see Figure C1.

$$z_{agl} = z_{rel} + z_{instr.} - z_{sfc} \tag{C1}$$

$z_{instr.}$ is the altitude of the instrument above mean sea level including the altitude of the instrument above the surface (building height or similar). z_{sfc} denotes the surface altitude of the receptor point at the location $p(x, y, t_{dw})$ and is used as STILT input. In this particular study we find differences of 150 m in altitude, if the topography is not accounted for. This corresponds to a difference in the weighting factors in the order of several percent. It is to be expected, that this error propagates more or less linear through the forward model (calculation of the enhancements using an emission inventory) will have deviations in a similar order of magnitude, if neglected. Please note, that the STILT model can also accept altitudes relative to mean sea level instead of surface elevation if kmsl-parameter is set to 1.

Appendix D: Calculation of the vertical weighting factor

As shown in Figure C1 the total column measurement integrates the molecules along the line of sight (yellow). We define along this line of sight STILT receptor-poionts at several altitudes q up to the maximum altitude q_{max}. The index $_r$ indicates receptors or the instruments point of view. Each of the receptor points represents a certain layer along the line of sight. The vertical weights w_q are calculated using the underlying meteorology as well as the EM27 instruments vertical column averaging kernel $A(z_r, t_r)$ at the receptor altitude z_r and receptor time t_r. e.g. (Hedelius et al., 2017, Fig. 5). The averaging kernel alters the weight in the order $\approx \pm 20\%$ depending on the time and altitude dependent solar elevation angle.

$$w_q = \frac{1}{w_\infty} \int\limits_{\hat{z}_{n-1}}^{\hat{z}_n} \rho(z_r) \cdot c_{gas}(z_r, t_r) \cdot A(z_r, t_r)\, dz \tag{D1}$$

Where as $w_\infty = \int_{z_{instr}}^{\infty} \rho(z_r) c_{gas}(z_r) A(z_r, t_r)\, dz$ represents the integral along the entire column and $c_{gas}(z_r)$ the vertical concentration profile of the target gas. $\hat{z}_n = 0.5(z_n + z_{n+1})$ denotes the midpoint between two receptor points. Here, we use the profile a-priori used for the total column retrieval. The upper most weight represents the entire residual atmosphere:

$$w_{q_{max}} = \frac{1}{w_\infty} \int\limits_{\hat{z}_q}^{\infty} \rho(z_r) \cdot c_{gas}(z_r, t_r) \cdot A(z_r, t_r)\, dz \tag{D2}$$

Appendix E: Discretisation of the upwind domain.

The upwind domain covered by the backward trajectories is discretised into a three-dimensional set of volumetric segments indexed by (i, j, k). The indices denote:

https://doi.org/10.5194/egusphere-2026-204
Preprint. Discussion started: 28 January 2026

- i: radial (upwind) distance bins,
- j: angular (wind-relative azimuth) sectors,
- k: vertical (altitude) layers.

Coordinates of a particle position are expressed in a local Cartesian system centered at the receptor (x_0, y_0) They are projected from geographic coordinates onto an appropriate map projection. For a particle at horizontal coordinates (x, y) and altitude z (above ground level), we define the horizontal polar coordinates

$$r(x,y) = \sqrt{(x-x_0)^2 + (y-y_0)^2}, \tag{E1}$$

$$\theta(x,y) = \operatorname{atan2}\bigl(y-y_0,\ x-x_0\bigr), \tag{E2}$$

where r is the radial distance and θ the azimuth measured in radians (convention: $-\pi < \theta \leq \pi$). To obtain wind-relative azimuths, the raw azimuth is rotated by a reference wind direction φ_{ref} (e.g., the mean wind direction during the analysed interval, measured clockwise from north), yielding

$$\theta' = \theta - \varphi_{\text{ref}}. \tag{E3}$$

The wind-relative angle θ' is then wrapped to the interval $(-\pi, \pi]$. The bin edges are defined by monotonically increasing sequences

$$0 = r_0 < r_1 < \cdots < r_{N_r},$$

$$-\pi = \theta'_0 < \theta'_1 < \cdots < \theta'_{N_\theta} = \pi,$$

$$z_0 < z_1 < \cdots < z_{N_z}.$$

where N_r, N_θ, N_z denote the number of radial, angular and vertical bins, respectively. A particle with coordinates (r, θ', z) is assigned to the segment with indices (i, j, k) if

$$r_i \leq r < r_{i+1}, \qquad \theta'_j \leq \theta' < \theta'_{j+1}, \qquad z_k \leq z < z_{k+1}. \tag{E4}$$

We define the *particle ensemble* associated with segment (i, j, k) as

$$P_{i,j,k} = \{\, p \mid \text{particle } p \text{ occupies cell } (i,j,k) \\ \text{at some model time step} \,\}. \tag{E5}$$

The residence time contributions of all particles in $P_{i,j,k}$ are accumulated to compute the segment footprint $f_{i,j,k}(t)$ and, after time-binning and vertical weighting, the transport kernel $k_{i,j,k}(t)$ (see Section 2.4).

https://doi.org/10.5194/egusphere-2026-204
Preprint. Discussion started: 28 January 2026

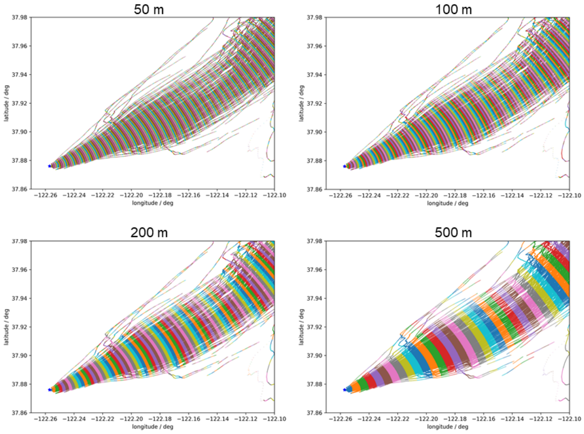

Figure F1. Illustration of various radial set definitions. The bin sizes range from 50m to 500m per step. Figure F2 shows that the method is largely independent on the choice of the bin size and thus not considered as a critical design parameter.

Appendix F: Impact of radial binning

We investigated the impact of multiple definitions of radial bins for the particles. Figure F1 illustrates the segmentation into 50,100,200 and 500m steps. We performed the fit described in section 2.5 for each of the segmentations. The resulting standard deviation of the fit residuals is shown in Figure F2. All of the sets find a minimum to 174, 304, 324, 350m with a mean of 288±68m. We conclude that the influence of the choice of the radial bins is negligible within bin sizes between 50 and 500m. However, some choices appear to create aliasing artifacts. We assume they average out over several events. In order to lower the computational effort we used a non-uniform radial discretization with exponentially increasing step sizes. This provides high spatial resolution near the origin while efficiently covering large radii. Optionally, a radius-dependent angular resolution is computed to maintain approximately isotropic (square) grid cells. However, the shape in the latitudinal-longitudinal domain plays a major role with respect to the derived transport kernel. Thus it is critical to define a segment, with entry- and exit-points mostly perpendicular to the particle trajectories. Radial binning ensures this in good approximation, especially in the near-field of the receptor.

Appendix G: Meteorological 4D field (HRRR)

The used meteorological model is the High-Resolution Rapid Refresh (HRRRv1) meteorological model (Blaylock et al., 2017; Pichugina et al., 2019, 2020). Despite the high spatial resolution of 3km^2, the complex topography as well as the land-sea conditions pose a major challenge to these meteorological models. Comparisons with a local meteorological site (LBNL1) indicate a good agreement, at least during the time of our observations.

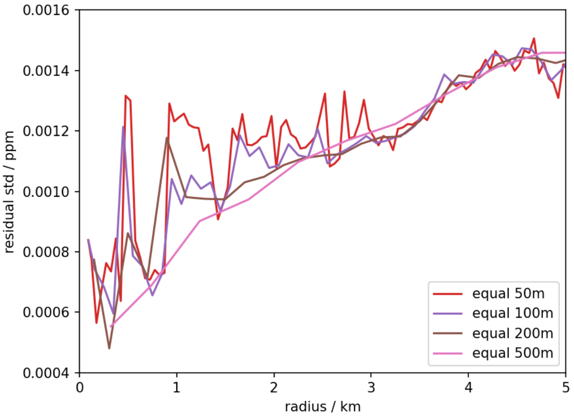

Figure F2. Standard deviation of the residual using the different radial segmentation sizes from 50m to 500m per step. The absolute minimum is similar for all choices of steps.

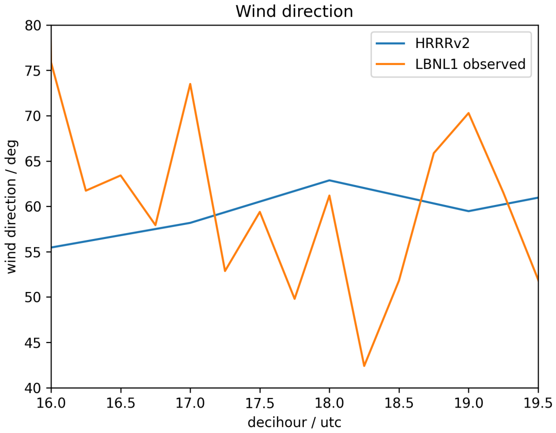

Figure G1. Comparison of wind direction.

Author contributions. The authors confirm contribution to the paper as follows: study conception and design: Jia Chen, Ronald C. Cohen, Jonathan Franklin, Steven Wofsy; data collection: Jia Chen, Ludwig Heinle, Hai Nquyen ; analysis and interpretation of results: Friedrich Klappenbach, Jia Chen, Ronald C. Cohen, Andreas Luther, Taylor Jones draft manuscript preparation: Friedrich Klappenbach All authors reviewed the results and approved the final version of the manuscript.

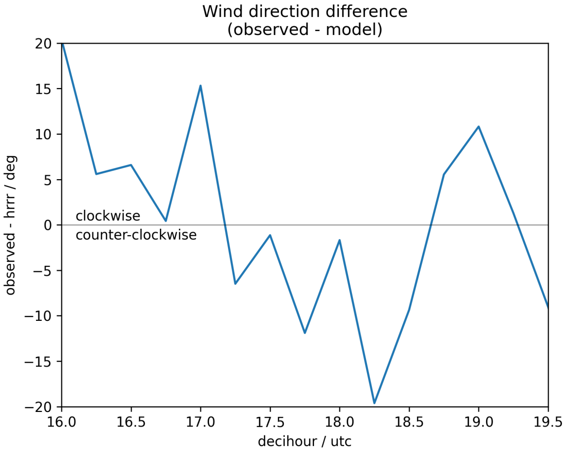

Figure G2. Difference in wind direction. Positive values indicate that the obtained source location might be found more in clockwise direction than the particles indicate.

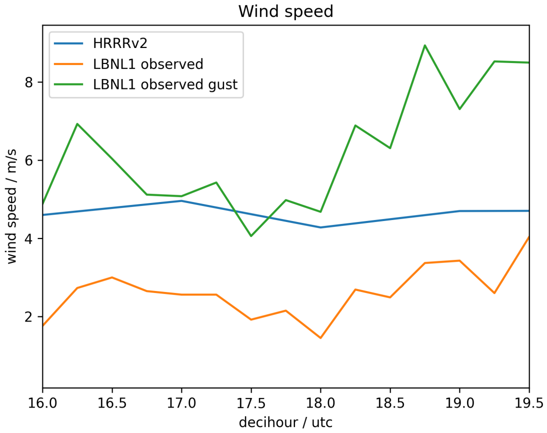

Figure G3. Comparison of wind speeds.

Competing interests. We declare that there are no competing interests associated with the research presented herein. We confirm that neither financial interests, personal relationships, nor any other conflicts of interest influenced the design, execution, or reporting of the findings in this work. All aspects of this research have been conducted with impartiality and solely for scientific inquiry.

345 *Acknowledgements.* This work has been funded by the ERC Consolidator Grant CoSense4Climate (grant no. 101089203, PI: Jia Chen), the European Union's Horizon 2020 Research and Innovation Programme under grant agreement no. 101037319 and BMFTR ITMS project (01LK2303B). Further, we acknowledge the maintainers of the meteorological site at Berkeley Lab, code 'LBNL1' for providing the ob-

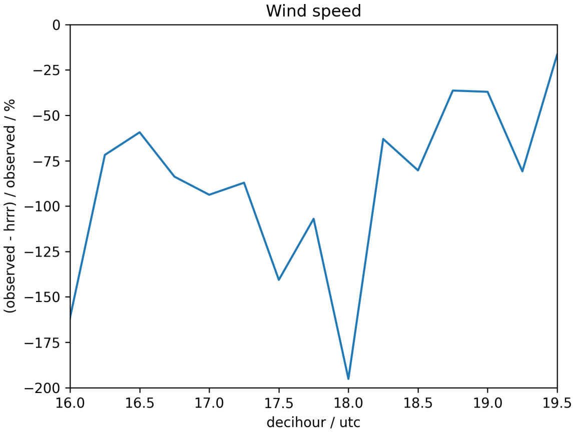

Figure G4. Comparison of wind speeds relative. The percentage gives the correction factor of the obtained source emission strengths.

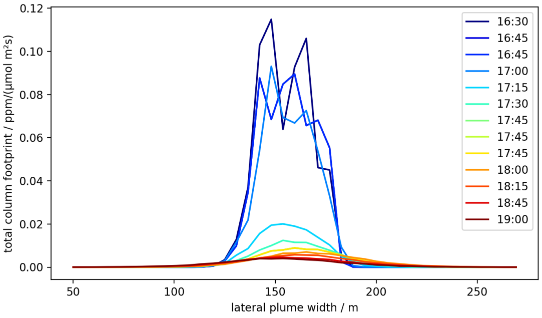

Figure G5. Lateral plume dispersion during the forenoon, approximately 130 m upwind of the receptor. While the plume remains narrow and well-defined earlier in the day, it broadens substantially later on. This widening directly leads to higher inferred emission estimates in the afternoon, even though the observed enhancement peaks remain nearly constant in both width and amplitude. .

servations nearby. We further acknowledge the hords of voluntary contributors to open source and/or free software, namely LaTeXas well as Python and its vast modules ’pandas’, ’matplotlib’, ’numpy’ and many implicit others.

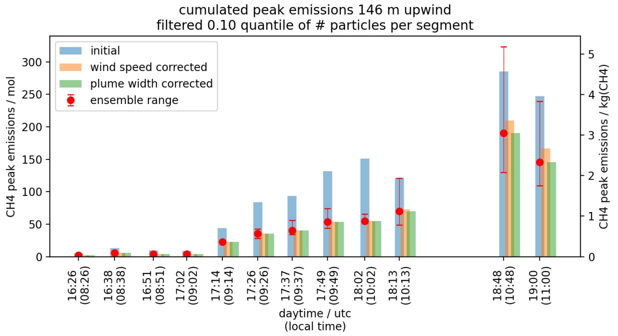

Figure G6. Impact of wind speed to the emission result and changes in plume upwind plume width. Note, first the wind speed correction is applied and the additionally plume width correction. The latter is found to have minimal impact on the emission result.

References

Al-Shalan, A., Lowry, D., Fisher, R., Nisbet, E., Zazzeri, G., Al-Sarawi, M., and France, J.: Methane emissions in Kuwait: Plume identification, isotopic characterisation and inventory verification, Atmospheric Environment, 268, 118 763, https://doi.org/10.1016/j.atmosenv.2021.118763, 2022.

Ammoura, L., Xueref-Remy, I., Vogel, F., Gros, V., Baudic, A., Bonsang, B., Delmotte, M., Té, Y., and Chevallier, F.: Exploiting stagnant conditions to derive robust emission ratio estimates for CO<sub>2</sub>, CO and volatile organic compounds in Paris, Atmospheric Chemistry and Physics, 16, 15 653–15 664, https://doi.org/10.5194/acp-16-15653-2016, 2016.

Andersen, T., Vinkovic, K., De Vries, M., Kers, B., Necki, J., Swolkien, J., Roiger, A., Peters, W., and Chen, H.: Quantifying methane emissions from coal mining ventilation shafts using an unmanned aerial vehicle (UAV)-based active AirCore system, Atmospheric Environment: X, 12, 100 135, https://doi.org/10.1016/j.aeaoa.2021.100135, 2021.

Barkley, Z. R., Lauvaux, T., Davis, K. J., Deng, A., Miles, N. L., Richardson, S. J., Cao, Y., Sweeney, C., Karion, A., Smith, M., Kort, E. A., Schwietzke, S., Murphy, T., Cervone, G., Martins, D., and Maasakkers, J. D.: Quantifying methane emissions from natural gas production in north-eastern Pennsylvania, Atmospheric Chemistry and Physics, 17, 13 941–13 966, https://doi.org/10.5194/acp-17-13941-2017, 2017.

Benjamin, S. G., Smirnova, T. G., Brown, J. M., Peckham, S. E., Grell, G. A., James, E. P., Weygandt, S. S., et al.: A North American hourly assimilation and model forecast cycle: The Rapid Refresh, Monthly Weather Review, 144, 1669–1694, https://doi.org/10.1175/MWR-D-15-0242.1, 2016a.

Benjamin, S. G., Weygandt, S. S., Brown, J. M., Hu, M., Alexander, C. R., Smirnova, T. G., James, E. P., Grell, G. A., Brundage, K. J., et al.: A North American hourly assimilation and model forecast cycle: The Rapid Refresh and High-Resolution Rapid Refresh, Noaa technical memorandum oar gsd-49, NOAA Earth System Research Laboratory, Global Systems Division, https://repository.library.noaa.gov/view/noaa/11429, 2016b.

Blaylock, B. K., Horel, J. D., and Liston, S. T.: Cloud archiving and data mining of High-Resolution Rapid Refresh forecast model output, Computers & Geosciences, 109, 43–50, https://doi.org/https://doi.org/10.1016/j.cageo.2017.08.005, 2017.

Chen, J., Viatte, C., Hedelius, J. K., Jones, T., Franklin, J. E., Parker, H., Gottlieb, E. W., Wennberg, P. O., Dubey, M. K., and Wofsy, S. C.: Differential column measurements using compact solar-tracking spectrometers, Atmospheric Chemistry and Physics, 16, 8479–8498, https://doi.org/10.5194/acp-16-8479-2016, 2016.

Chen, J., Dietrich, F., Maazallahi, H., Forstmaier, A., Winkler, D., Hofmann, M. E. G., Denier van der Gon, H., and Röckmann, T.: Methane emissions from the Munich Oktoberfest, Atmospheric Chemistry and Physics, 20, 3683–3696, https://doi.org/10.5194/acp-20-3683-2020, 2020.

Cui, Y. Y., Brioude, J., Angevine, W. M., Peischl, J., McKeen, S. A., Kim, S., Neuman, J. A., Henze, D. K., Bousserez, N., Fischer, M. L., Jeong, S., Michelsen, H. A., Bambha, R. P., Liu, Z., Santoni, G. W., Daube, B. C., Kort, E. A., Frost, G. J., Ryerson, T. B., Wofsy, S. C., and Trainer, M.: Top-down estimate of methane emissions in California using a mesoscale inverse modeling technique: The San Joaquin Valley, Journal of Geophysical Research: Atmospheres, 122, 3686–3699, https://doi.org/10.1002/2016JD026398, 2017.

Desjardins, R., Worth, D., Pattey, E., VanderZaag, A., Srinivasan, R., Mauder, M., Worthy, D., Sweeney, C., and Metzger, S.: The challenge of reconciling bottom-up agricultural methane emissions inventories with top-down measurements, Agricultural and Forest Meteorology, 248, 48–59, https://doi.org/10.1016/j.agrformet.2017.09.003, 2018.

Dietrich, F., Chen, J., Voggenreiter, B., Aigner, P., Nachtigall, N., and Reger, B.: MUCCnet: Munich Urban Carbon Column network, Atmospheric Measurement Techniques, 14, 1111–1126, https://doi.org/10.5194/amt-14-1111-2021, 2021.

Dietrich, F., Chen, J., Shekhar, A., Lober, S., Krämer, K., Leggett, G., van der Veen, C., Velzeboer, I., Denier van der Gon, H., and Röckmann, T.: Climate Impact Comparison of Electric and Gas-Powered End-User Appliances, Earth's Future, 11, e2022EF002 877, https://doi.org/https://doi.org/10.1029/2022EF002877, e2022EF002877 2022EF002877, 2023.

Enishi, O.: Greenhouse gas emissions caused from livestock in Japan, in: Proceedings of the 4th Workshop on Greenhouse Gas Inventories in Asia Jakarta,(GGIAJ, 2007), National Institute for Environmental Studies, Japan, 2007.

Fairley, D. and Fischer, M. L.: Top-down methane emissions estimates for the San Francisco Bay Area from 1990 to 2012, Atmospheric Environment, 107, 9–15, https://doi.org/10.1016/j.atmosenv.2015.01.065, 2015.

Fasoli, B., Lin, J. C., Bowling, D. R., Mitchell, L., and Mendoza, D.: Simulating atmospheric tracer concentrations for spatially distributed receptors: updates to the Stochastic Time-Inverted Lagrangian Transport model's R interface (STILT-R version 2), Geoscientific Model Development, 11, 2813–2824, https://doi.org/10.5194/gmd-11-2813-2018, 2018.

Feld, L., Herkommer, B., Vestner, J., Dubravica, D., Alberti, C., and Hase, F.: PROFFASTpylot: Running PROFFAST with Python, Journal of Open Source Software, 9, 6481, https://doi.org/10.21105/joss.06481, 2024.

Forstmaier, A., Chen, J., Dietrich, F., Bettinelli, J., Maazallahi, H., Schneider, C., Winkler, D., Zhao, X., Jones, T., Van Der Veen, C., Wildmann, N., Makowski, M., Uzun, A., Klappenbach, F., Denier Van Der Gon, H., Schwietzke, S., and Röckmann, T.: Quantification of methane emissions in Hamburg using a network of FTIR spectrometers and an inverse modeling approach, Atmospheric Chemistry and Physics, 23, 6897–6922, https://doi.org/10.5194/acp-23-6897-2023, 2023.

Frey, M., Sha, M. K., Hase, F., Kiel, M., Blumenstock, T., Harig, R., Surawicz, G., Deutscher, N. M., Shiomi, K., Franklin, J. E., Bösch, H., Chen, J., Grutter, M., Ohyama, H., Sun, Y., Butz, A., Tsidu, G. M., Ene, D., Wunch, D., Cao, Z., Garcia, O., Ramonet, M., Vogel, F., and Orphal, J.: Building the COllaborative Carbon Column Observing Network (COCCON): long-term stability and ensemble performance of the EM27/SUN Fourier transform spectrometer, Atmos. Meas. Tech., p. 18, 2019.

Gisi, M., Hase, F., Dohe, S., and Blumenstock, T.: Camtracker: a new camera controlled high precision solar tracker system for FTIR-spectrometers, Atmospheric Measurement Techniques, 4, 47–54, https://doi.org/10.5194/amt-4-47-2011, 2011.

Gisi, M., Hase, F., Dohe, S., Blumenstock, T., Simon, A., and Keens, A.: XCO<sub>2</sub>-measurements with a tabletop FTS using solar absorption spectroscopy, Atmospheric Measurement Techniques, 5, 2969–2980, https://doi.org/10.5194/amt-5-2969-2012, 2012.

Hamburg, S., Gautam, R., and Zavala-Araiza, D.: MethaneSAT - A New Tool Purpose-Built to Measure Oil and Gas Methane Emissions from Space, in: Day 1 Mon, October 31, 2022, p. D011S007R002, SPE, Abu Dhabi, UAE, https://doi.org/10.2118/210922-MS, 2022.

Hase, F.: COCCON Data Processing (last access: 2026-01-08), https://www.imk-asf.kit.edu/english/3225.php, 2025.

Hase, F., Frey, M., Kiel, M., Blumenstock, T., Harig, R., Keens, A., and Orphal, J.: Addition of a channel for XCO observations to a portable FTIR spectrometer for greenhouse gas measurements, Atmospheric Measurement Techniques, 9, 2303–2313, https://doi.org/10.5194/amt-9-2303-2016, 2016.

Hedelius, J. K., Parker, H., Wunch, D., Roehl, C. M., Viatte, C., Newman, S., Toon, G. C., Podolske, J. R., Hillyard, P. W., Iraci, L. T., Dubey, M. K., and Wennberg, P. O.: Intercomparability of X_{CO_2} and X_{CH_4} from the United States TCCON sites, Atmospheric Measurement Techniques, 10, 1481–1493, https://doi.org/10.5194/amt-10-1481-2017, 2017.

Hegarty, R. S., Goopy, J. P., Herd, R. M., and McCorkell, B.: Cattle selected for lower residual feed intake have reduced daily methane production1,2, Journal of Animal Science, 85, 1479–1486, https://doi.org/10.2527/jas.2006-236, 2007.

Hopkins, F. M., Ehleringer, J. R., Bush, S. E., Duren, R. M., Miller, C. E., Lai, C.-T., Hsu, Y.-K., Carranza, V., and Randerson, J. T.: Mitigation of methane emissions in cities: How new measurements and partnerships can contribute to emissions reduction strategies: URBAN METHANE MITIGATION, Earth's Future, 4, 408–425, https://doi.org/10.1002/2016EF000381, 2016.

Hu, H., Hasekamp, O., Butz, A., Galli, A., Landgraf, J., Aan De Brugh, J., Borsdorff, T., Scheepmaker, R., and Aben, I.: The operational methane retrieval algorithm for TROPOMI, Atmospheric Measurement Techniques, 9, 5423–5440, https://doi.org/10.5194/amt-9-5423-2016, 2016.

Hu, H., Landgraf, J., Detmers, R., Borsdorff, T., Aan De Brugh, J., Aben, I., Butz, A., and Hasekamp, O.: Toward Global Mapping of Methane With TROPOMI: First Results and Intersatellite Comparison to GOSAT, Geophysical Research Letters, 45, 3682–3689, https://doi.org/10.1002/2018GL077259, 2018.

Jones, T. S., Franklin, J. E., Chen, J., Dietrich, F., Hajny, K. D., Paetzold, J. C., Wenzel, A., Gately, C., Gottlieb, E., Parker, H., Dubey, M., Hase, F., Shepson, P. B., Mielke, L. H., and Wofsy, S. C.: Assessing urban methane emissions using column-observing portable Fourier transform infrared (FTIR) spectrometers and a novel Bayesian inversion framework, Atmospheric Chemistry and Physics, 21, 13 131–13 147, https://doi.org/10.5194/acp-21-13131-2021, 2021.

Karion, A., Lauvaux, T., Lopez Coto, I., Sweeney, C., Mueller, K., Gourdji, S., Angevine, W., Barkley, Z., Deng, A., Andrews, A., Stein, A., and Whetstone, J.: Intercomparison of atmospheric trace gas dispersion models: Barnett Shale case study, Atmospheric Chemistry and Physics, 19, 2561–2576, https://doi.org/10.5194/acp-19-2561-2019, 2019.

Lassey, K. R.: Livestock methane emission and its perspective in the global methane cycle, Australian Journal of Experimental Agriculture, 48, 114, https://doi.org/10.1071/EA07220, 2008.

Lebel, E. D., Finnegan, C. J., Ouyang, Z., and Jackson, R. B.: Methane and NO $_x$ Emissions from Natural Gas Stoves, Cooktops, and Ovens in Residential Homes, Environmental Science & Technology, 56, 2529–2539, https://doi.org/10.1021/acs.est.1c04707, 2022.

Lin, J. C., Gerbig, C., Wofsy, S. C., Andrews, A. E., Daube, B. C., Davis, K. J., and Grainger, C. A.: A near-field tool for simulating the upstream influence of atmospheric observations: The Stochastic Time-Inverted Lagrangian Transport (STILT) model, Journal of Geophysical Research: Atmospheres, 108, https://doi.org/https://doi.org/10.1029/2002JD003161, 2003.

Loughner, C. P., Fasoli, B., Stein, A. F., and Lin, J. C.: Incorporating features from the Stochastic Time-Inverted Lagrangian Transport (STILT) model into the Hybrid Single-Particle Lagrangian Integrated Trajectory (HYSPLIT) model: a unified dispersion model for time-forward and time-reversed applications, Journal of Applied Meteorology and Climatology, https://doi.org/10.1175/jamc-d-20-0158.1, 2021.

Luther, A., Kleinschek, R., Scheidweiler, L., Defratyka, S., Stanisavljevic, M., Forstmaier, A., Dandocsi, A., Wolff, S., Dubravica, D., Wildmann, N., Kostinek, J., Jöckel, P., Nickl, A.-L., Klausner, T., Hase, F., Frey, M., Chen, J., Dietrich, F., Nęcki, J., Swolkień, J., Fix, A., Roiger, A., and Butz, A.: Quantifying CH<sub>4</sub> emissions from hard coal mines using mobile sun-viewing Fourier transform spectrometry, Atmospheric Measurement Techniques, 12, 5217–5230, https://doi.org/10.5194/amt-12-5217-2019, 2019.

Makarova, M. V., Alberti, C., Ionov, D. V., Hase, F., Foka, S. C., Blumenstock, T., Warneke, T., Virolainen, Y., Kostsov, V., Frey, M., Poberovskii, A. V., Timofeyev, Y. M., Paramonova, N., Volkova, K. A., Zaitsev, N. A., Biryukov, E. Y., Osipov, S. I., Makarov, B. K., Polyakov, A. V., Ivakhov, V. M., Imhasin, H. K., and Mikhailov, E. F.: Emission Monitoring Mobile Experiment (EMME): an overview and first results of the St. Petersburg megacity campaign-2019, preprint, Gases/Remote Sensing/Instruments and Platforms, https://doi.org/10.5194/amt-2020-87, 2020.

Makowski, M., Hase, F., Klappenbach, F., Luther, A., Feld, L., Müller, M., Giridharan, V., Fait, C., and Chen, J.: EM27 Retrieval Pipeline, https://doi.org/10.5281/zenodo.14284968, 2025.

Myhre, G., Shindell, D., Bréon, F.-M., Collins, W., Fuglestvedt, J., Huang, J., Koch, D., Lamarque, J.-F., Lee, D., Mendoza, B., Nakajima, T., Robock, A., Stephens, G., Takemura, T., and Zhang, H.: Anthropogenic and natural radiative forcing, pp. 659–740, Cambridge University Press, Cambridge, UK, https://doi.org/10.1017/CBO9781107415324.018, 2013.

Mønster, J., Kjeldsen, P., and Scheutz, C.: Methodologies for measuring fugitive methane emissions from landfills – A review, Waste Management, 87, 835–859, https://doi.org/10.1016/j.wasman.2018.12.047, 2019.

Patel, M. Y., Zhu, Y., Winter, A. R., Asimow, N. G., and Cohen, R. C.: Plume Detection and Emissions Quantification Potential Using a Dense Sensor Network, ACS ES&T Air, 2, 1099–1106, https://doi.org/10.1021/acsestair.5c00069, 2025.

Pichugina, Y. L., Banta, R. M., Bonin, T., Brewer, W. A., Choukulkar, A., McCarty, B. J., Baidar, S., Draxl, C., Fernando, H. J. S., Kenyon, J., Krishnamurthy, R., Marquis, M., Olson, J., Sharp, J., and Stoelinga, M.: Spatial Variability of Winds and HRRR–NCEP Model Error Statistics at Three Doppler-Lidar Sites in the Wind-Energy Generation Region of the Columbia River Basin, Journal of Applied Meteorology and Climatology, 58, 1633–1656, https://doi.org/10.1175/JAMC-D-18-0244.1, 2019.

Pichugina, Y. L., Banta, R. M., Alan Brewer, W., Bianco, L., Draxl, C., Kenyon, J., Lundquist, J. K., Olson, J. B., Turner, D. D., Wharton, S., Wilczak, J., Baidar, S., Berg, L. K., Fernando, H. J. S., McCarty, B. J., Rai, R., Roberts, B., Sharp, J., Shaw, W. J., Stoelinga, M. T., and Worsnop, R.: Evaluating the WFIP2 updates to the HRRR model using scanning Doppler lidar measurements in the complex terrain of the Columbia River Basin, Journal of Renewable and Sustainable Energy, 12, 043 301, https://doi.org/10.1063/5.0009138, 2020.

Schneising, O., Burrows, J. P., Dickerson, R. R., Buchwitz, M., Reuter, M., and Bovensmann, H.: Remote sensing of fugitive methane emissions from oil and gas production in North American tight geologic formations, Earth's Future, 2, 548–558, https://doi.org/10.1002/2014EF000265, 2014.

Sha, M. K., De Mazière, M., Notholt, J., Blumenstock, T., Chen, H., Dehn, A., Griffith, D. W. T., Hase, F., Heikkinen, P., Hermans, C., Hoffmann, A., Huebner, M., Jones, N., Kivi, R., Langerock, B., Petri, C., Scolas, F., Tu, Q., and Weidmann, D.: Intercomparison of low- and high-resolution infrared spectrometers for ground-based solar remote sensing measurements of total column concentrations of CO 2 , CH 4 , and CO, Atmospheric Measurement Techniques, 13, 4791–4839, https://doi.org/10.5194/amt-13-4791-2020, 2020.

Shekhar, A., Chen, J., Paetzold, J. C., Dietrich, F., Zhao, X., Bhattacharjee, S., Ruisinger, V., and Wofsy, S. C.: Anthropogenic CO $_2$ emissions assessment of Nile Delta using XCO $_2$ and SIF data from OCO-2 satellite, Environmental Research Letters, 15, 095 010, https://doi.org/10.1088/1748-9326/ab9cfe, 2020.

Solazzo, E., Crippa, M., Guizzardi, D., Muntean, M., Choulga, M., and Janssens-Maenhout, G.: Uncertainties in the Emissions Database for Global Atmospheric Research (EDGAR) emission inventory of greenhouse gases, Atmospheric Chemistry and Physics, 21, 5655–5683, https://doi.org/10.5194/acp-21-5655-2021, 2021.

Stein, A. F., Draxler, R. R., Rolph, G. D., Stunder, B. J. B., Cohen, M. D., and Ngan, F.: NOAA's HYSPLIT Atmospheric Transport and Dispersion Modeling System, Bulletin of the American Meteorological Society, 96, 2059–2077, https://doi.org/10.1175/BAMS-D-14-00110.1, 2015.

Subramanian, R., Williams, L. L., Vaughn, T. L., Zimmerle, D., Roscioli, J. R., Herndon, S. C., Yacovitch, T. I., Floerchinger, C., Tkacik, D. S., Mitchell, A. L., Sullivan, M. R., Dallmann, T. R., and Robinson, A. L.: Methane Emissions from Natural Gas Compressor Stations in the Transmission and Storage Sector: Measurements and Comparisons with the EPA Greenhouse Gas Reporting Program Protocol, Environmental Science & Technology, 49, 3252–3261, https://doi.org/10.1021/es5060258, 2015.

Thorpe, A. K., Duren, R. M., Conley, S., Prasad, K. R., Bue, B. D., Yadav, V., Foster, K. T., Rafiq, T., Hopkins, F. M., Smith, M. L., Fischer, M. L., Thompson, D. R., Frankenberg, C., McCubbin, I. B., Eastwood, M. L., Green, R. O., and Miller, C. E.: Methane emissions from underground gas storage in California, Environmental Research Letters, 15, 045 005, https://doi.org/10.1088/1748-9326/ab751d, 2020.

Viatte, C., Lauvaux, T., Hedelius, J. K., Parker, H., Chen, J., Jones, T., Franklin, J. E., Deng, A. J., Gaudet, B., Verhulst, K., Duren, R., Wunch, D., Roehl, C., Dubey, M. K., Wofsy, S., and Wennberg, P. O.: Methane emissions from dairies in the Los Angeles Basin, Atmospheric Chemistry and Physics, 17, 7509–7528, https://doi.org/10.5194/acp-17-7509-2017, 2017.

Vogel, F. R., Frey, M., Staufer, J., Hase, F., Broquet, G., Xueref-Remy, I., Chevallier, F., Ciais, P., Sha, M. K., Chelin, P., Jeseck, P., Janssen, C., Té, Y., Groß, J., Blumenstock, T., Tu, Q., and Orphal, J.: XCO<sub>2</sub> in an emission hot-spot region: the COCCON Paris campaign 2015, Atmospheric Chemistry and Physics, 19, 3271–3285, https://doi.org/10.5194/acp-19-3271-2019, 2019.

Wu, D., Lin, J. C., Fasoli, B., Oda, T., Ye, X., Lauvaux, T., Yang, E. G., and Kort, E. A.: A Lagrangian approach towards extracting signals of urban CO_2 emissions from satellite observations of atmospheric column CO_2 (XCO_2): X-Stochastic Time-Inverted Lagrangian Transport model ("X-STILT v1"), Geoscientific Model Development, 11, 4843–4871, https://doi.org/10.5194/gmd-11-4843-2018, publisher: Copernicus GmbH, 2018.

Wunch, D., Toon, G. C., Sherlock, V., Deutscher, N. M., Liu, C., Feist, D. G., and Wennberg, P. O.: Documentation for the 2014 TCCON Data Release, https://data.caltech.edu/records/249, publisher: CaltechDATA, 2015.

Xueref-Remy, I., Zazzeri, G., Bréon, F., Vogel, F., Ciais, P., Lowry, D., and Nisbet, E.: Anthropogenic methane plume detection from point sources in the Paris megacity area and characterization of their δ13C signature, Atmospheric Environment, 222, 117 055, https://doi.org/10.1016/j.atmosenv.2019.117055, 2020.

Young, H. A., Turnbull, J. C., Keller, E. D., Domingues, L. G., Parry-Thompson, J., Hilton, T. W., Brailsford, G. W., Gray, S., Moss, R. C., and Mikaloff-Fletcher, S.: Urban flask measurements of CO $_2$ ff and CO to identify emission sources at different site types in Auckland, New Zealand, Philosophical Transactions of the Royal Society A: Mathematical, Physical and Engineering Sciences, 381, 20220 204, https://doi.org/10.1098/rsta.2022.0204, 2023.